Materials Horizons

COMMUNICATION

View Article Online
View Journal

Cite this: DOI: 10.1039/c9mh00272c

Received 20th February 2019,
Accepted 10th May 2019

DOI: 10.1039/c9mh00272c

rsc.li/materials-horizons

Robust production of 2D quantum sheets from bulk layered materials†

Yuanqing Xu,[ab] Shulin Chen,[cd] Zhipeng Dou,[ce] Yanhong Ma,[a] Yang Mi,[f] Wenna Du,[f] Yin Liu,[g] Jianqi Zhang,[a] Jinquan Chang,[a] Cheng Liang,[a] Jin Zhou,[a] Hongbo Guo,[h] Peng Gao,[cij] Xinfeng Liu,[f] Yanke Che[g] and Yong Zhang*[ab]

The production of two-dimensional quantum sheets (2D QSs) from bulk layered materials is highly desired but far from satisfactory. Herein, we report a unified top-down method capable of producing a range of 2D QSs in high yields. The method combines silica-assisted ball-milling and sonication-assisted solvent exfoliation and thus enables production of graphene QSs (GQSs), boron nitride QSs (BNQSs), molybdenum disulfide QSs (MoS_2 QSs), and tungsten disulfide QSs (WS_2 QSs) in exceedingly high yields of 35.5, 33.6, 30.2, and 28.2 wt%, respectively. The as-produced 2D QSs are confirmed as intrinsic and defect-free by multiple characterization techniques. Such 2D QSs can be collected as powders and then redispersed in a wide range of solvents with high concentration up to 5 mg mL^{-1}. Both (re)dispersions and solid thin films of the 2D QSs exhibit extraordinarily high performance in linear and nonlinear optics. Specifically, the QS (re)dispersions show prominent exciton-, solvent-, and concentration-dependent photoluminescence, while the QS solid thin films demonstrate exciting solid-state fluorescence (with lifetimes up to 3.0 ns) and remarkable nonlinear absorption saturation (with absolute modulation depths up to 59% and saturation intensities down to 6.70 kW cm^{-2} (0.67 nJ cm^{-2})). Our method could be applicable to any bulk layered materials and therefore paves the way for mass production and full exploration of 2D QSs.

New concepts

The production of 2D QSs with intrinsic and defect-free characteristics is highly desired for exploration of their primary performances and identification of the underlying mechanisms. Meanwhile, high-universality and high-yield production of 2D QSs is highly required for construction of their complete library based on identical protocols and criteria. We demonstrate the simultaneous achievement of high universality, high yield, and high quality during 2D QS production *via* a creatively unified top-down method. This method provides a standard platform for the construction of the complete library of 2D QSs, and therefore greatly prompts the mass production and full exploration of such intriguing materials.

Introduction

Two-dimensional (2D) materials, since their discovery,[1,2] have been intensively explored owning to their unique properties in electronics,[3] optics,[4] magnetism,[5] catalysis,[6] and so on.[7] However, most of the exploration has been devoted to 2D micro/nanosheets (NSs).[8,9] With lateral sizes down to the sub-20 nm regime, 2D quantum sheets (QSs) have emerged.[10] By integration of the intrinsic characteristics of 2D materials together with quantum confinement and prominent edge effects, 2D

[a] CAS Key Laboratory of Nanosystem and Hierarchical Fabrication, CAS Center for Excellence in Nanoscience, National Center for Nanoscience and Technology, Beijing 100190, P. R. China. E-mail: zhangyong@nanoctr.cn
[b] University of Chinese Academy of Sciences, Beijing 100049, P. R. China
[c] Electron Microscopy Laboratory, School of Physics, Peking University, Beijing 100871, P. R. China
[d] State Key Laboratory of Advanced Welding and Joining, Harbin Institute of Technology, Harbin 150001, P. R. China
[e] Key Laboratory for Micro-/Nano-Optoelectronic Devices of Ministry of Education, School of Physics and Electronics, Hunan University, Changsha 410082, P. R. China
[f] CAS Key Laboratory of Standardization and Measurement for Nanotechnology, CAS Center for Excellence in Nanoscience, National Center for Nanoscience and Technology, Beijing 100190, P. R. China
[g] CAS Key Laboratory of Photochemistry, CAS Research/Education Center for Excellence in Molecular Sciences, Institute of Chemistry, Chinese Academy of Sciences, Beijing 100190, P. R. China
[h] CAS Key Laboratory for Biomedical Effects of Nanomaterials and Nanosafety, CAS Center for Excellence in Nanoscience, National Center for Nanoscience and Technology, Beijing 100190, P. R. China
[i] Collaborative Innovation Center of Quantum Matter, Beijing 100871, P. R. China
[j] International Center for Quantum Materials, School of Physics, Peking University, Beijing 100871, P. R. China

† Electronic supplementary information (ESI) available. See DOI: 10.1039/c9mh00272c

QSs have attracted increasing attention recently.[11–13] To fully exploit the properties of 2D QSs, mass production of such intriguing materials is highly required. Both bottom-up[14] and top-down[15,16] methods have been employed for the production of 2D QSs. So far, none of them is satisfactory because they are restricted either by rigorous conditions and tedious post-treatment or by extremely low yields. Another challenge towards the current methods is to produce 2D QSs with intrinsic and defect-free characteristics.

Compared with bottom-up methods, top-down methods are preferable thanks to the abundance of bulk layered materials.[17] Top-down methods enable the production of 2D QSs directly from bulk layered materials through the successive breakage of in-plane chemical bonds and interlayer van der Waals interactions. It is known that sonication and ball-milling, as well as grinding, can be used to exfoliate and pulverize bulk layered materials.[11,12] However, the transformation of bulk layered materials into 2D QSs is far from satisfactory. Meanwhile, a unified method capable of producing a range of 2D QSs from bulk layered materials is highly desired. Surprisingly, little progress has been made until recently.[13] Despite the universality of the reported method, the production yield and (re)dispersion concentration are disappointing. We have newly proposed a top-down method through a sequential combination of salt-assisted ball-milling and sonication-assisted solvent exfoliation.[11] Such a method has shown great success in the production of 2D QSs from transition metal dichalcogenides (TMDs). However, the discouraging attempt at producing 2D QSs from graphite and hexagonal boron nitride has clearly identified the specialism of the proposed method.

To date, a method that can achieve high universality and high yield simultaneously is still lacking, which in turn highlights the significance and imminence of such an ultimate method. Herein, we report a unified top-down method that combines silica-assisted ball-milling and sonication-assisted solvent exfoliation. The method enabled reproducible production of a range of 2D QSs in high yields. To testify its generalism and robustness, graphite, hexagonal boron nitride, molybdenum disulfide, and tungsten disulfide were selected as the most representative bulk layered materials. Without exception, graphene QSs (GQSs), boron nitride QSs (BNQSs), molybdenum disulfide QSs (MoS_2 QSs), and tungsten disulfide QSs (WS_2 QSs) were produced in extremely high yields of 35.5, 33.6, 30.2, and 28.2 wt%, respectively. The as-produced 2D QSs were structurally characterized as intrinsic and defect-free. Extraordinary solvent diversity and solvability were demonstrated towards the redispersion of the 2D QSs. The as-obtained QS (re)dispersions showed prominent photoluminescence (PL) with exciton-, solvent-, and concentration-dependency. The solution-processed QSs–poly(methyl methacrylate) (PMMA) hybrid thin films presented exciting solid-state fluorescence and remarkable nonlinear absorption saturation.

Results and discussion

To elucidate the proposed unified top-down method, a schematic was briefly drawn. As shown in Fig. 1a, through

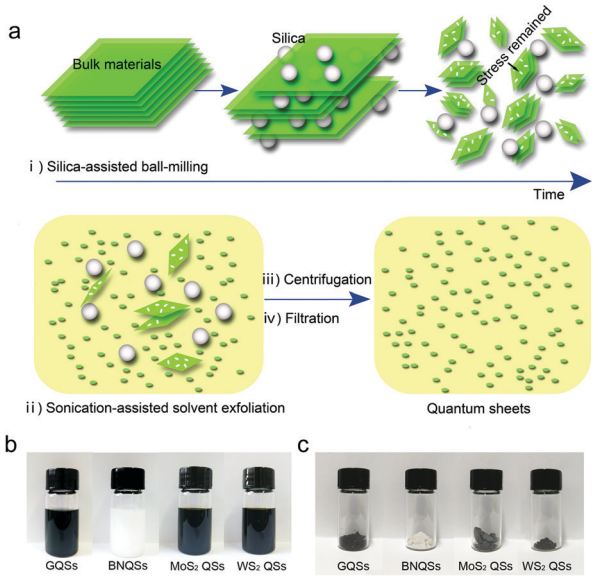

Fig. 1 Unified top-down method for production of 2D QSs. (a) Schematic illustration of the fabrication process. (b) Photographs of the as-obtained QS dispersions. (c) Photographs of the as-collected QS powders.

sequential combination of silica-assisted ball-milling and sonication-assisted solvent exfoliation, highly efficient transformation from bulk layered materials into 2D QSs was realized. A single cycle of the fabrication process enabled production of GQSs, BNQSs, MoS_2 QSs, and WS_2 QSs from their bulk layered materials (Fig. S1, ESI†) with extremely high yields of 35.5, 33.6, 30.2, and 28.2 wt%, respectively, which were 1–2 orders of magnitude higher than those reported previously.[12,13] Compared with our recent work,[11] the production yields for MoS_2 and WS_2 QSs were improved by 18% and 40% respectively. High universality and high yield were, for the first time, simultaneously achieved. This was a highly desired breakthrough and hence a complete library of 2D QSs could be constructed based on identical protocols and criteria. To identify the underlying mechanism, a thorough comparison to our recent work[11] was conducted. The ultimate shift from specialism to generalism of the top-down method could be originated from the simple replacement of the inorganic salt (*i.e.*, sodium chloride) by silica microspheres. The silica microspheres showed several unique features such as high uniformity, smooth surface, and high stability (Fig. S2, ESI†), significantly facilitating the silica-assisted ball-milling process (Fig. S3, ESI†). The perfect matching between the silica microspheres and agate milling ball in density and hardness (as well as constituent) enabled maximum reproducibility and long-term stability of the production process. The dual synergy effect of the milling balls and silica microspheres resulted in unprecedented maximization of the pulverization and exfoliation of bulk layered materials (Fig. S3, ESI†). The following sonication-assisted solvent exfoliation further exfoliated the as-milled materials into mono/few layers, which were then tailored into 2D QSs under sonication triggered by the remaining stress.

As reported in our recent work,[11] during the salt-assisted ball-milling process, the sodium chloride remained cubic

crystallites with average sizes of approximately 1–3 μm. Assuming that the compression forces during the ball-milling at 500 rpm were transferred through the opposite faces of the sodium chloride crystallites, the calculated pressure on the 2D material surfaces was 4–36 GPa. Considering the probability of transferring the compression forces through the sharp edges and even the corners of the sodium chloride crystallites, the 2D material surfaces could eventually receive an average pressure well above the reported breaking strength of TMDs (*e.g.*, 16–30 GPa for MoS_2),[18] which led to the great success in the production of MoS_2 and WS_2 QSs. However, it was beyond the capacity of salt-assisted ball-milling to pulverize graphite and hexagonal boron nitride at an acceptable level because of their much higher breaking strengths (130 GPa for monolayer graphene[19] and 70 GPa for few-layer boron nitride[20]) than that of TMDs. Unlike salt-assisted ball-milling, silica-assisted ball-milling achieved unprecedented success in the production of 2D QSs from not only TMDs but also graphite and hexagonal boron nitride. Silica microspheres (450 nm in diameter) allowed for significantly sharp contact with the 2D material surface, indicating the achievement of unprecedentedly high pressure on the 2D material surface. For example, with silica microspheres as the transfer media for the compression forces (500 rpm), the calculated pressure on the 2D material surfaces through circular contact (presumed radius of 100 nm) was 1146 GPa, well above the breaking strengths of graphite, hexagonal boron nitride, and TMDs,[18–20] indicating the determinative contribution of silica-assisted ball-milling in the success of the unified top-down method.

Fig. 1b presents the initial dispersions (approximately 1.5 mg mL^{-1}) of the 2D QSs in *N*-methyl-2-pyrrolidone (NMP) except for BNQSs in mixed (1 : 1 v/v) solvents of NMP and isopropanol (IPA). No detectable precipitation was observed when standing still for 7 days, indicating the high stability of the initial dispersions. Fig. 1c demonstrates the as-collected QS powders (approximately 1 gram for each). By sequential combination of solvent precipitation and centrifugation separation, the powder collection process could be efficiently conducted (Fig. S4, ESI†). Solvent diversity and solvability towards redispersion of 2D QSs is shown in Fig. S5 (ESI†). Specifically, GQSs could be readily redispersed in water, ethanol, IPA, acetone, dimethylformamide (DMF), tetrahydrofuran (THF), and NMP respectively with high concentrations ranging from 3 to 5 mg mL^{-1}, which were 2–3 orders of magnitude higher than that reported previously.[13] BNQSs and MoS_2 QSs, however, presented distinct solvent-selectivity (*e.g.*, water and ethanol for BNQSs while water, IPA, DMF, and NMP for MoS_2 QSs). Zeta potentials were measured to be −26.3, −40.3, and −31.7 mV for GQS, BNQS, and MoS_2 QS aqueous redispersions (0.1 mg mL^{-1}) respectively, demonstrating their satisfactory stability (Fig. S6, ESI†).

The as-produced 2D QSs were characterized by using multiple microscopic techniques. Fig. 2a–c showed transmission electron microscopy (TEM) images of well-dispersed 2D QSs with uniform shapes and sizes. From the insets, the lateral size distributions of 3.2 ± 0.6, 1.9 ± 0.4, and 2.1 ± 0.6 nm were

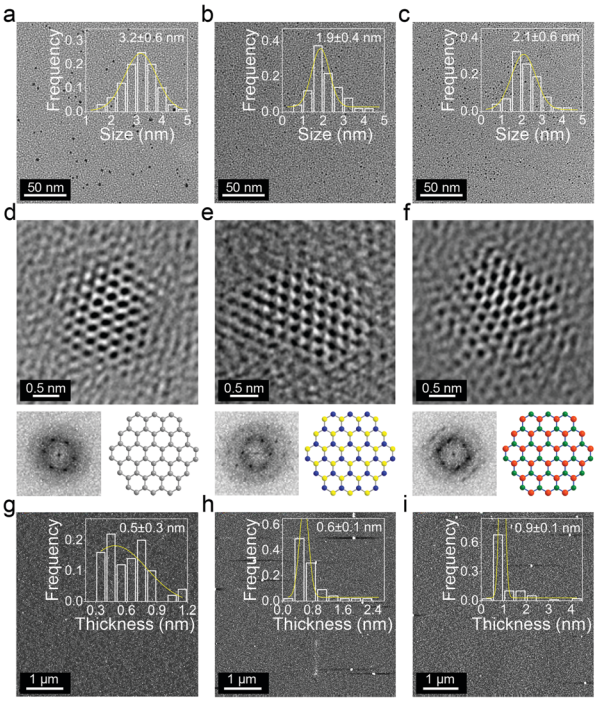

Fig. 2 Microscopic characterization of the 2D QSs. (a)–(c) TEM images of GQSs (a), BNQSs (b), and MoS_2 QSs (c), respectively (insets showing the lateral size distributions). (d)–(f) HRTEM images of GQSs (d), BNQSs (e), and MoS_2 QSs (f), respectively (bottom panels showing the corresponding FFT patterns and structure diagrams). (g)–(i) AFM images of GQSs (g), BNQSs (h), and MoS_2 QSs (i), respectively (insets showing the height distributions).

derived for GQSs, BNQSs, and MoS_2 QSs respectively. Single QSs were structurally revealed by high-resolution TEM (HRTEM, Fig. 2d–f) which clearly identified the nature of crystalline (structure diagrams were shown for clarity). Note that HRTEM demonstrated trigonal prismatic (2H) rather than octahedral (1T) phase in MoS_2 QSs, which could be determinative of their electronic and optical properties.[9] The corresponding fast Fourier transform (FFT) patterns confirmed their single-crystalline characteristics. Both HRTEM and FFT indicated the intrinsic structures of the 2D QSs. From atomic force microscopy (AFM, Fig. 2g–i) images, height distributions of 0.5 ± 0.3, 0.6 ± 0.1, and 0.9 ± 0.1 nm were obtained for GQSs, BNQSs, and MoS_2 QSs respectively. Evidently the 2D QSs were atomically thin with approximately 1–2 layers, based on the consideration that the thicknesses of single-layer graphene, boron nitride, and MoS_2 were 0.34, 0.35, and 0.65 nm respectively.

Multiple spectroscopic techniques were employed for further characterization of the as-produced 2D QSs. Fig. 3a–c shows the UV-vis spectra of GQSs, BNQSs, and MoS_2 QSs respectively. Quantum confinement and prominent edge effects were responsible for the distinct absorption performances between QSs and NSs. Meanwhile, diverse spectral shapes were presented for 2D QSs. For GQSs, the absorption peak at approximately 267 nm was attributed to the π–π* transition of the sp^2 basal plane.[15] Unlike GQSs, BNQSs showed no detectable absorption peaks above 270 nm in the UV-vis region. For MoS_2

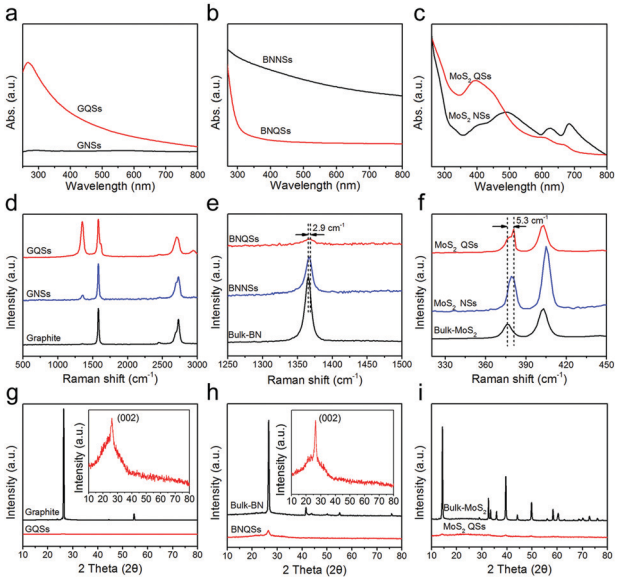

Fig. 3 Spectroscopic characterization of the 2D QSs. (a)–(c) UV-vis absorption spectra. (d)–(f) Raman spectra. (g)–(i) XRD patterns. Data for 2D NSs and bulk materials are shown for comparison.

QSs, significant blue shift of the characteristic peaks was observed, demonstrating the remarkable quantum confinement effect.[11] Raman spectra of the 2D QSs are shown in Fig. 3d–f. For GNSs, the G band at around 1582 cm^{-1} was originated from the E_{2g} phonon vibrational mode in the center of the Brillouin zone, whereas the D band near 1356 cm^{-1} was assigned to the breathing mode of sp^2 C atoms.[21] Compared with graphite and GNSs, significantly increased I_D/I_G ratio (0.93) in GQSs indicated an unprecedented level of exfoliation and pulverization from the unified top-down method, resulting in quantum confinement and prominent edge effects. Compared with bulk BN and BNNSs, the E_{2g} phonon mode at around 1369 cm^{-1} in the BNQSs was greatly suppressed, suggesting the successful exfoliation and size-reduction into 2D QSs.[16] For bulk MoS_2, the E^1_{2g} mode at 376 cm^{-1} and A_{1g} mode at 403 cm^{-1} were clearly observed. The apparent blue shift of the E^1_{2g} mode in the MoS_2 QSs was similar to the mode change of black phosphorus quantum dots with thickness and lateral size reduction.[22] The X-ray diffraction (XRD) technique was applied to further identify the crystalline structures of the 2D QSs. As shown in Fig. 3g–i, the bulk layered materials demonstrated their distinct characteristic peaks corresponding to specific inter/intralayer crystal faces, whereas the 2D QSs presented significantly suppressed responses due to the greatly reduced inter/intralayer domains.[13] The remaining detectable single peaks at $\sim 26^\circ$ in the insets (Fig. 3g and h) resulted from the (002) crystal faces of the GQSs and BNQSs, respectively. X-ray photoelectron spectroscopy (XPS) was performed to further identify the defect-free characteristics of the 2D QSs. As shown in Fig. S12 (ESI†), the spectra of the GQSs and BNQSs demonstrated no observable oxidation or other functionalization,[15,16] supporting their intrinsic and defect-free structures. In the spectra of the MoS_2 QSs, the trace amount of Mo^{6+} at 235.9 eV indicated negligible oxidation of Mo edge atoms.[11]

From the above, a range of 2D QSs was produced with high yield and large quantity *via* the unified top-down method; meanwhile the as-produced 2D QSs were intrinsic and defect-free, which provided a highly reliable platform for systematic investigation of their properties. Fig. 4 presents the PL performance of the 2D QS dispersions. GQS, BNQS, and MoS_2 QS dispersions, without exception, demonstrated significant exciton-dependent PL behavior, as shown in Fig. 4a–f. With 360 nm laser irradiation, strong blue fluorescence was emitted from the GQSs/NMP (0.01 mg mL^{-1}), BNQSs/H_2O (1 mg mL^{-1}), and MoS_2 QSs/NMP (0.01 mg mL^{-1}) dispersions, respectively (insets, Fig. 4a–c). Both intensity and wavelength of PL were dependent on the excitation wavelength (Fig. 4d–f). The PL intensity reached the maximum at 360, 380, and 380 nm for GQSs/NMP, BNQSs/H_2O, and MoS_2 QSs/NMP dispersions, respectively, whereas the PL wavelength gradually red-shifted with increasing excitation wavelength. Such exciton-dependent PL behavior could be originated from the size-/thickness-heterogeneity of the 2D QSs.[23] Fig. 4g–i present the remarkable concentration-dependent PL behavior of the 2D QS dispersions.

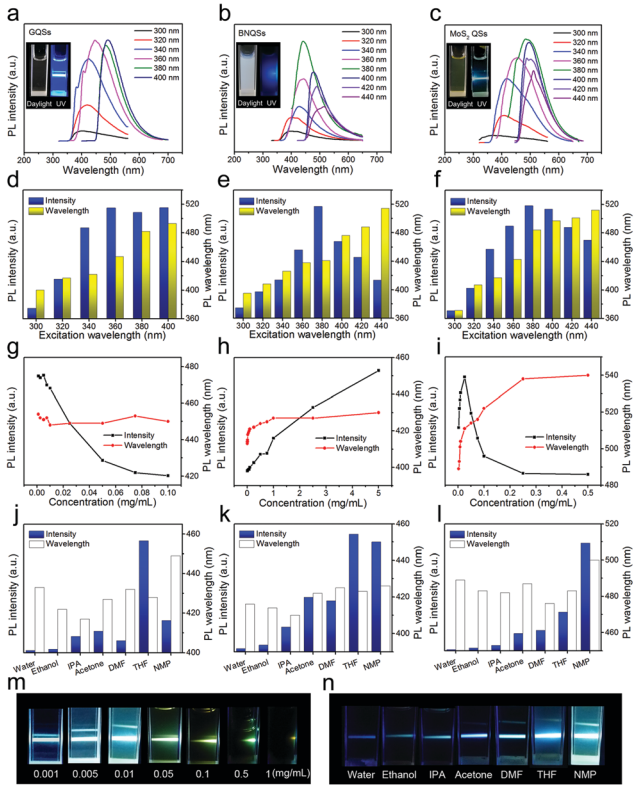

Fig. 4 Photoluminescence of the QS dispersions. (a)–(c) PL spectra of the GQSs/NMP (a), BNQSs/H_2O (b), and MoS_2 QSs/NMP (c) dispersions respectively at varying excitation wavelengths. Insets are photographs of the QS dispersions under daylight and 360 nm laser irradiation. (d)–(f) Exciton-dependent PL behavior. (g)–(i) Concentration-dependent PL behavior. (j)–(l) Solvent-dependent PL behavior. The concentration is fixed at 0.01 mg mL^{-1}. The excitation wavelength for the GQS (g and j), BNQS (h and k), and MoS_2 QS (i and l) dispersions is 360 nm, 330 nm, and 380 nm respectively. (m and n) Photographs of the MoS_2 QS dispersions with varying concentrations (m) and solvents (n) under 360 nm laser irradiation.

For the GQSs/NMP dispersions, the PL intensity decreased dramatically with increasing concentrations, whereas the PL wavelength demonstrated negligible variation at approximately 450 nm after the initial slight blue-shift (Fig. 4g). Such concentration-induced PL quenching in the GQSs/NMP dispersions was probably driven by the aggregation-caused quenching (ACQ) mechanism,[24] which widely exists in aromatic compounds with rigid π–π conjugated basal planes (structural analogues to GQSs). Meanwhile, the observed concentration-quenching effect was a firm indication of the bandgap fluorescence mechanism[25] (usually applied in intrinsic and defect-free 2D QSs) for the GQSs/NMP dispersions. Both mechanisms facilitated the non-radiative decay of the excited states due to the enhanced QS–QS interactions by possible interlayer stacking when concentrated, therefore resulting in PL quenching. It should be noted that self-absorption of the emitted PL by the GQSs in the dispersions could contribute to the PL quenching as well. Therefore, the observed PL quenching by concentration could be the combined contribution from the non-radiative decay of the excited states and the self-absorption of the emitted PL. Fig. 4h demonstrates the concentration-dependent PL behavior for the BNQSs/H_2O dispersions. The PL intensity increased progressively with increasing concentrations (up to 5 mg mL^{-1}), whereas the PL wavelength rapidly red-shifted from purple to blue. Such concentration-caused PL enhancement in the BNQSs/H_2O dispersions was similar to aggregation-induced emission (AIE),[24] which has been extensively exploited in aromatic compounds with rotatable intramolecular single bonds. However, such similarity in the phenomena was driven by distinct mechanisms (*e.g.*, restriction of intramolecular rotation (RIR) for AIE) because of the dissimilar structures between BNQSs and AIE luminogens. Meanwhile, the bandgap fluorescence mechanism for the GQSs/NMP dispersions was not applicable to the BNQSs/H_2O dispersions because of the absence of PL quenching by concentration. Based on the above considerations, the edge-derived fluorescence mechanism[25] was indicated for the BNQSs/H_2O dispersions, which allowed for steady growth of the PL intensity due to the enhanced edge–edge interactions between approaching BNQSs with increasing concentrations. Besides the increased QS–QS interactions (through edges), the decreased QS–solvent interactions (through direct contact of free edges to solvent molecules) contributed to the PL enhancement as well, due to the reduced energy/charge transfer into the solvents (surroundings).[23] From Fig. 3a–c, unlike GQSs and MoS_2 QSs, BNQSs demonstrated negligible absorption in the visible range, leading to minimized self-absorption effects on the PL intensities, ensuring the steady growth of the PL intensity. Fig. 4i presents the concentration-dependent PL behavior for the MoS_2 QSs/NMP dispersions. The PL intensity increased proportionally with concentration (up to 0.01 mg mL^{-1}) at the initial stage simply because of the increase of the PL emitters. After reaching the maximum, the PL intensity demonstrated concentration-induced PL quenching driven by a similar mechanism to that of GQSs/NMP dispersions. The PL wavelength gradually red-shifted from blue to green, showing much broader fluorescence modulation by concentration compared with the GQSs/NMP and BNQSs/H_2O dispersions. The possible interlayer stacking with increasing concentrations would probably result in the decreasing of the bandgap of MoS_2 QSs, leading to the apparent red shift of the PL. Besides the non-radiative decay of the excited states and the self-absorption of the emitted PL, the possible transition from direct-gap (single-layer) to indirect-gap (few-layer) MoS2 QSs[26] by interlayer stacking with increasing concentrations could be responsible to the PL quenching as well. Fig. 4j–l demonstrate the solvent-dependent PL behavior of the 2D QS dispersions. Despite the randomly distributed PL wavelength, the PL intensity presented constructive and destructive effects in THF/NMP (aprotic solvents) and H_2O/ethanol (protic solvents), respectively.[23] The negatively charged edges/surfaces (Fig. S6, ESI†) enabled protonation/solvation of the 2D QSs by the protic solvents, which maximized the non-radiative decay of the excited states through energy/charge transfer into the solvents (surroundings), therefore resulting in the PL quenching in H_2O/ethanol. In contrast, the weak interactions between the 2D QSs and aprotic solvents facilitated the radiative routes of the excited states, and therefore induced the PL enhancement in THF/NMP. The PL (absolute) quantum yields of the 2D QS dispersions were generally lower than 10% and could be regulated as well through varying QS–solvent interactions[23] (Fig. S15, ESI†). Fig. 4m and n show photographs of the MoS_2 QS dispersions with varying concentrations and solvents irradiated by a 360 nm laser, which were direct visualizations of Fig. 4i and l respectively.

By solution processing, QSs–PMMA hybrid thin films were readily fabricated. Fig. 5a (top panel) presents the as-fabricated hybrid thin films with a loading content of 0.1 wt%. Both TEM and small-angle X-ray scattering (SAXS) images (Fig. 5a (bottom panel) and Fig. S16 and S17, ESI†) confirmed the uniform and random dispersion (*i.e.*, no detectable aggregation and orientation) of 2D QSs in PMMA. Meanwhile, such dispersion was thermodynamically stable in the QSs–PMMA thin films where the radius of gyration of the linear PMMA was greater than the radius of the 2D QS.[27] Fig. 5b demonstrates the solid-state fluorescence (with excitation wavelength of 360 nm) of the QSs–PMMA thin films with varying loading contents. The PL intensity, as well as wavelength, showed similar trends to the corresponding QS dispersions with varying concentrations, which suggested the same mechanisms for both dispersions and thin films. Notably, the BNQSs–PMMA thin films presented exponentially growing PL intensity, undoubtedly identifying the strong QS–QS interactions (through edges) therefore firmly supporting the edge-derived fluorescence mechanism. Compared with the NSs–PMMA, the QSs–PMMA (with identical loading content of 0.2 wt%) exhibited significantly higher PL intensity, firmly indicating the quantum confinement and prominent edge effects, which were the origins for the bandgap fluorescence and edge-derived fluorescence, respectively.[25] Fig. 5c presents the 3D histogram from which the fluorescence intensities with varying QSs and loading contents were directly comparable. Evidently, the MoS_2 QSs–PMMA showed superior solid-state fluorescence to those of GQSs–PMMA and BNQSs–PMMA with loading contents from 0.1 to 1 wt%. However, the

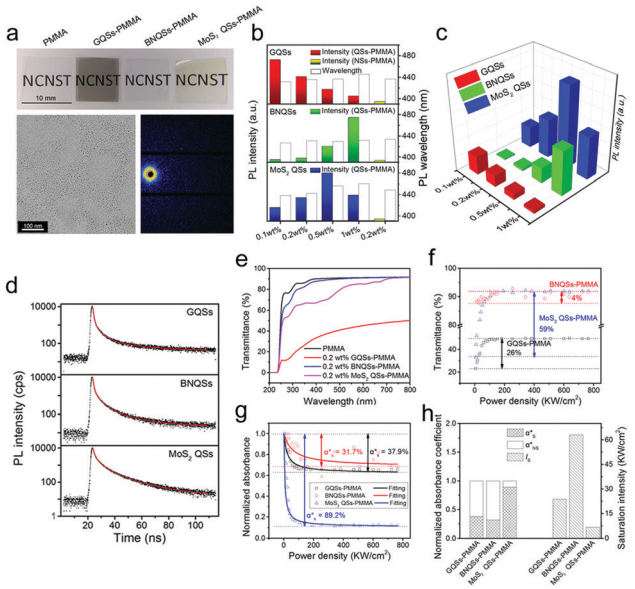

Fig. 5 Fluorescence and NLO performance of the QS solid thin films. (a) (top panel) Photographs of the QSs–PMMA hybrid thin films (0.1 wt%); (bottom panel) TEM image of the (GQSs–PMMA) cross-section and corresponding SAXS image. (b) Solid-state fluorescence of the QSs–PMMA thin films at the excitation wavelength of 360 nm. (c) 3D histogram showing direct comparison of fluorescence intensities with varying QSs and loading contents. (d) Time-resolved PL decay profile of the QSs–PMMA thin films (0.5 wt%) upon 370 nm excitation wavelength. (e), UV-vis absorption spectra of the QSs–PMMA thin films (0.2 wt%). (f) Nonlinear saturable absorption curves. (g) Normalized absorption curves. The hollow dots are the experimental data, and the solid curves are analytical fits to the data. (h) Plots of the normalized absorption coefficient and saturation intensity. The incident laser beam was as follows: wavelength of 800 nm, pulse of 100 fs, and repetition rate of 1 kHz.

BNQSs–PMMA demonstrated exponential growth of solid-state fluorescence and overtook the MoS_2 QSs–PMMA at a loading content of 1 wt%. As for the GQSs–PMMA, the solid-state fluorescence could be enhanced by edge functionalization,[10] which would induce additional edge-derived fluorescence. The solid-state fluorescence lifetimes were obtained by simulation of the time-resolved PL decay profiles (Fig. 5d). The QSs–PMMA thin films (0.5 wt%) demonstrated lifetimes of 1.4, 1.7, and 3.0 ns for GQSs–PMMA, BNQSs–PMMA, and MoS_2 QSs–PMMA, respectively. The acquisition of ns-scale exciton radiative lifetimes, nearly 3 orders of magnitude longer than that reported previously,[13] was exciting thanks to the quantum confinement and prominent edge effects of the 2D QSs.[28] Solid-state fluorescence of 2D QSs was highly desired but rarely achieved before. Its discovery in QSs–PMMA thin films relied on the unprecedented level of dispersion of 2D QSs in PMMA.

Not only the fluorescence but also the nonlinear optical (NLO) performances of the QSs–PMMA thin films were investigated. Fig. 5e–h presents the linear and nonlinear optical absorption respectively. Apparently, the UV-vis spectra (Fig. 5e) of the thin films (0.2 wt%) showed excellent consistency with the direct observation of the thin films (0.1 wt%, Fig. 5a, top panel). Considering that the thicknesses of the thin films were 8 μm, and assuming that the densities of the thin films (0.2 wt%) were similar to that of pure PMMA (1.18×10^3 mg mL^{-1}), the linear absorption coefficients (at 800 nm) were calculated to be 2.6×10^4, 4.4×10^3, and 4.6×10^3 mL mg^{-1} m^{-1} for GQSs–PMMA, BNQSs–PMMA, and MoS_2 QSs–PMMA, respectively, larger than those reported for 2D NS dispersions.[8,21] Fig. 5f presents the nonlinear saturable absorption (NSA) curves of the QSs–PMMA thin films with the femtosecond laser at an illumination wavelength of 800 nm. The thin films with identical loading contents of 0.2 wt% showed distinct NSA performances with (absolute) modulation depths of 26%, 4%, and 59% for GQSs–PMMA, BNQSs–PMMA, and MoS_2 QSs–PMMA, respectively. Such remarkable modulation depth of nearly 60% was rarely achieved except for monolayer graphene.[11,29–34] Compared with monolayer graphene,[30] the MoS_2 QSs–PMMA thin film demonstrated bright prospects thanks to its unique features such as solution-processability, designable flexibility, and robust modulation. The first demonstration of such exceptionally large modulation depth in 2D QSs would facilitate their potential applications in photonics, lasers, and nonlinear optics. Fig. 5g shows the normalized NSA curves of the QSs–PMMA thin films. The experimental data were perfectly fitted by using the following formula: $\alpha^*(I) = \alpha_S^*/(1 + I/I_S) + \alpha_{NS}^*$ where $\alpha^*(I)$ was the absorption coefficient, α_S^* and α_{NS}^* were the saturable and nonsaturable absorption components, I was the peak intensity (or power density) of the incident pulsed laser, and I_S was the saturation intensity defined as the optical intensity required in a steady state to reduce the absorption to half of its unbleached value.[29] From the fitting, the (relative) modulation depths (*i.e.*, α_S^*) of 37.9%, 31.7%, and 89.2% were derived for GQSs–PMMA, BNQSs–PMMA, and MoS_2 QSs–PMMA, respectively. Fig. 5h presents plots of the normalized absorption coefficients and saturation intensities. Evidently, the MoS_2 QSs–PMMA demonstrated the best NSA performance in the three as-examined hybrid thin films. In addition, the saturation intensities of 23.8, 63.0, and 6.70 kW cm^{-2} (*i.e.*, 2.38, 6.30, and 0.67 nJ cm^{-2}) were derived for GQSs–PMMA, BNQSs–PMMA, and MoS_2 QSs–PMMA, respectively, which were at least 1–2 orders of magnitude lower than those reported previously.[11,29–34] The simultaneous achievement of remarkable modulation depths and extraordinary saturation intensities in QSs–PMMA would prompt the full exploration of the 2D QSs.

Conclusions

In summary, we have achieved the reproducible production of a range of intrinsic and defect-free 2D QSs in high yields through a highly unified top-down method. By sequential combination of silica-assisted ball-milling and sonication-assisted solvent exfoliation, GQSs, BNQSs, MoS_2 QSs, and WS_2 QSs were produced from their bulk layered materials in exceptionally high yields (> 28 wt%), with approximately 1–2 orders of magnitude improvement compared with the current production methods. Extraordinary solvent diversity and solvability enabled the as-desired redispersion of the 2D QSs, which greatly facilitated the solution processing towards hybrid thin films. Outstanding exciton-,

solvent-, and concentration-dependent PL performances were demonstrated for the QS dispersions. The possible mechanisms such as bandgap fluorescence and edge-derived fluorescence were proposed for both dispersions and thin films. The discovery of solid-state fluorescence with ns-scale lifetimes in QSs–PMMA would undoubtedly expedite their practical applications. The QSs–PMMA further demonstrated phenomenal NSA performances with absolute modulation depths up to nearly 60% and saturation intensities down to sub-10 kW cm^{-2} (sub-1 nJ cm^{-2}), suggesting their potential applications in mode-locked lasers and related fields. Our method provided an unprecedented standard platform for construction of the ultimate complete library of 2D QSs, and therefore would significantly boost the mass production and full exploration of such intriguing materials.

Methods

Materials

Graphite (flake), hexagonal boron nitride (powder), and molybdenum disulfide (powder) were purchased from Sigma Aldrich. Tungsten disulfide (powder) was purchased from Aladdin Industrial Corporation. Porous anodic alumina (PAA) (0.02 μm pore size) and nylon (220 nm pore size) filters were purchased from Whatman. *N*-Methyl-2-pyrrolidone (NMP), dimethylformamide (DMF), and tetraethyl orthosilicate (TEOS) were purchased from Shanghai Macklin Biochemical Co., Ltd. Tetrahydrofuran (THF), acetone, isopropanol (IPA), ethanol, ethyl acetate, and aqueous ammonia (25.0–28.0%) were purchased from Beijing Chemical Works. All of the materials were used as received. Deionized water was used in the experiments.

Synthesis of silica microspheres

Silica microspheres (approximately 450 nm in diameter) were synthesized *via* a typical Stöber process.[35] In brief, 200 mL ethanol was added into a three-necked 500 mL flask. The system was magnetically stirred and heated to 70 °C through an oil bath, followed by the addition of 40 mL TEOS. 20 minutes later, 40 mL aqueous ammonia and 40 mL deionized water were added and stirred for 2 hours. When the system was cooled down to room temperature, the silica was immediately precipitated by centrifugation (4500 rpm, 10 min) (Centrifuge, Z32 HK, HERMLE). The supernatant was discarded, and the rest was washed with ethanol. After several cycles (centrifugation-discard-washing), the silica was vacuum-dried to a powder.

Production of 2D QSs in dispersions

In a typical fabrication process of 2D QSs, bulk powder (0.7 g), silica microspheres (7 g) and 3 mm agate balls (70 g) were mixed and put into an agate jar for ball-milling (Planetary ball mill, QM-3SP04, Nanjing LaiBu Technology Industry Co., Ltd) at 500 rpm for 12 h. The powder mixture was separated from the agate balls by the screen mesh (pore size 1 mm). The as-separated mixture was dispersed in NMP (NMP–IPA (1 : 1, v/v) was used for boron nitride) with concentration of approximately 55 mg mL^{-1} (*i.e.*, 5 mg mL^{-1} for the bulk powder concentration) for sonication (Vibra-Cell Ultrasonic Liquid Processor, VCX800, SONICS) at 240 W for 5 h. The dispersion was treated by centrifugation at 4500 rpm for 30 min (silica microspheres were completely precipitated). The upper 2/3 liquid was then treated by vacuum filtration (Chemistry diaphragm pump, MD4C NT, Vacuubrand) through a 0.02 μm PAA membrane. The filtrate was collected as the 2D QS dispersion.

Redispersion of 2D QSs

The redispersion process is schematically illustrated in Fig. S4 (ESI†). The 2D QS initial dispersions were highly stable under ambient conditions. To collect 2D QS powders, poor solvent (*n*-hexane) and cosolvent (IPA for GQSs, MoS_2 QSs, and WS_2 QSs, while ethyl acetate for BNQSs) was added into the initial dispersions by the optimized volume ratio (*e.g.*, initial dispersion/poor solvent/cosolvent = 5/10/2). By standing still overnight or accelerated centrifugation (6000 rpm, 30 min), 2D QSs were efficiently precipitated from the initial dispersions. After discarding the supernatant, the rest was dried into powders. The production yield was calculated by the weight ratio between the 2D QS powder and the bulk powder. High yields of approximately 35.5, 33.6, 30.2, and 28.2 wt% were obtained for GQSs, BNQSs, MoS_2 QSs and WS_2 QSs, respectively. By simple sonication, the as-collected 2D QS powders could be redispersed in a wide range of solvents with high concentrations.

Fabrication of QSs–PMMA thin films

Solution processing was used for the fabrication of QSs–PMMA thin films. In brief, PMMA was dissolved in NMP to form a 150 mg mL^{-1} solution by magnetic stirring overnight at increased temperature. Meanwhile, the QS powders were dispersed in NMP (H_2O for BNQSs) to form a 5 mg mL^{-1} dispersion by sonication. The PMMA solution and QS dispersion was mixed based on the pre-designed loading contents and the as-required constant total weight (PMMA + QS) by vigorous stirring and sonication. The mixture with known volume was dropped into a PTFE mold (a 8 μm thick polyimide film as the releasing layer). After complete removal of the solvent from the evenly spreading mixture by moderate heating (70 °C) overnight on a hot plate, the QSs–PMMA thin films were obtained.

Production of 2D NSs

The 2D NSs were produced by liquid exfoliation of bulk layered materials.[8,21] In brief, bulk layered materials were dispersed in solvents (NMP for graphite, MoS_2, and WS_2, while IPA for boron nitride) with concentration of 5 mg mL^{-1}, followed by sonication at 240 W for 5 h. The resulting dispersions were then treated by centrifugation at 1500 rpm for 10 min. 2D NSs in the upper 2/3 liquid were collected by vacuum filtration through a 220 nm nylon membrane, followed by washing with ethanol several times. The filter cakes were vacuum-dried to 2D NS powders.

Characterization

Transmission electron microscopy (TEM) images were acquired using an FEI Tecnai G2 20 ST microscope operated at 200 kV.

High-resolution TEM (HRTEM) images were acquired using an aberration-corrected FEI Titan Cubed Themis G2 microscope operated at 300 kV. Atomic force microscopy (AFM) images were acquired using a Bruker MultiMode 8 AFM using SCANASYST-AIR cantilevers with a nominal tip radius of 2 nm in a scanasyst mode. Scanning electron microscopy (SEM) images were acquired using a Hitachi S-4800 microscope. Zeta potential measurements were conducted using a Malvern Zetasizer Nano ZS analyzer. UV-vis absorption spectra were recorded using a Lambda 950 spectrophotometer from PerkinElmer. Raman spectra were recorded using a Renishaw inVia plus spectrometer with a 514 nm laser. X-ray diffraction (XRD) patterns were recorded using D/Max-TTRIII (CBO) with Cu Kα radiation (λ = 1.54056 Å). X-ray photoelectron spectroscopy (XPS) measurements were conducted using an ESCALAB 250Xi electron spectrometer from VG Scientific with 300 W Al Kα radiation. Photoluminescence (PL) measurements were conducted using a HORIBA Jobin Yvon NanoLog-TCSPC spectrofluorometer with varying excitation wavelengths. PL quantum yields were measured by the integrating sphere method using a Hamamatsu Absolute PL Quantum Yield spectrometer C11347-11. Small-angle X-ray scattering (SAXS) measurements were performed at the Xeuss WAXS/SAXS system (λ = 1.54 Å). Scattered X-rays were detected by using a Dectris Pilatus R 300K photon counting detector. Nonlinear absorption measurements were performed with 100 fs pulses from a Coherent Astrella regenerative amplifier. The laser was operated at 800 nm wavelength with a pulse repetition rate of 1 kHz. All photographs were acquired with a digital camera.

Conflicts of interest

The authors declare no competing interests.

Acknowledgements

This work was supported by a grant (No. 61575049) from the National Natural Science Foundation of China, the 100-Talent Program of Chinese Academy of Sciences, the start-up funding from the National Center for Nanoscience and Technology, the National Natural Science Foundation of China (grant numbers 51502007 and 51672007), the National Basic Research Program of China (grant numbers 2016YFA0300804 and 2016YFA0300903), and "2011 Program" Peking-Tsinghua-IOP Collaborative Innovation Center of Quantum Matter. We gratefully acknowledge the Electron Microscopy Laboratory at Peking University for the use of the Cs corrected electron microscope.

References

1 K. S. Novoselov, A. K. Geim, S. V. Morozov, D. Jiang, Y. Zhang, S. V. Dubonos, I. V. Grigorieva and A. A. Firsov, Electric field effect in atomically thin carbon films, *Science*, 2004, **306**, 666.

2 K. S. Novoselov, D. Jiang, F. Schedin, T. J. Booth, V. V. Khotkevich, S. V. Morozov and A. K. Geim, Two-dimensional atomic crystals, *Proc. Natl. Acad. Sci. U. S. A.*, 2005, **102**, 10451.

3 G. Fiori, F. Bonaccorso, G. Iannaccone, T. Palacios, D. Neumaier, A. Seabaugh, S. K. Banerjee and L. Colombo, Electronics based on two-dimensional materials, *Nat. Nanotechnol.*, 2014, **9**, 768.

4 F. Xia, H. Wang, D. Xiao, M. Dubey and A. Ramasubramaniam, Two-dimensional material nanophotonics, *Nat. Photonics*, 2014, **8**, 899.

5 O. V. Yazyev, Emergence of magnetism in graphene materials and nanostructures, *Rep. Prog. Phys.*, 2010, **73**, 056501.

6 D. Deng, K. S. Novoselov, Q. Fu, N. Zheng, Z. Tiang and X. Bao, Catalysis with two-dimensional materials and their heterostructures, *Nat. Nanotechnol.*, 2016, **11**, 218.

7 F. Bonaccorso, L. Colombo, G. Yu, M. Stoller, V. Tozzini, A. C. Ferrari, R. S. Ruoff and V. Pellegrini, Graphene, related two-dimensional crystals, and hybrid systems for energy conversion and storage, *Science*, 2015, **347**, 1246501.

8 J. N. Coleman, M. Lotya, A. O'Neill, S. D. Bergin, P. J. King, U. Khan, K. Young, A. Gaucher, S. De, R. J. Smith, I. V. Shvets, S. K. Arora, G. Stanton, H. Y. Kim, K. Lee, G. T. Kim, G. S. Duesberg, T. Hallam, J. J. Boland, J. J. Wang, J. F. Donegan, J. C. Grunlan, G. Moriarty, A. Shmeliov, R. J. Nicholls, J. M. Perkins, E. M. Grieveson, K. Theuwissen, D. W. McComb, P. D. Nellist and V. Nicolosi, Two-dimensional nanosheets produced by liquid exfoliation of layered materials, *Science*, 2011, **331**, 568.

9 M. Chhowalla, H. S. Shin, G. Eda, L. J. Li, K. P. Loh and H. Zhang, The chemistry of two-dimensional layered transition metal dichalcogenide nanosheets, *Nat. Chem.*, 2013, **5**, 263.

10 X. Wang, G. Sun, N. Li and P. Chen, Quantum dots derived from two-dimensional materials and their applications for catalysis and energy, *Chem. Soc. Rev.*, 2016, **45**, 2239.

11 C. Han, Y. Zhang, P. Gao, S. Chen, X. Liu, Y. Mi, J. Zhang, Y. Ma, W. Jiang and J. Chang, High-yield production of MoS_2 and WS_2 quantum sheets from their bulk materials, *Nano Lett.*, 2017, **17**, 7767.

12 X. Zhang, Z. Lai, Z. Liu, C. Tan, Y. Huang, B. Li, M. Zhao, L. Xie, W. Huang and H. Zhang, A facile and universal top-down method for preparation of monodisperse transition-metal dichalcogenide nanodots, *Angew. Chem., Int. Ed.*, 2015, **54**, 5425.

13 Y. Wang, Y. Liu, J. Zhang, J. Wu, H. Xu, X. Wen, X. Zhang, C. S. Tiwary, W. Yang, R. Vajtai, Y. Zhang, N. Chopra, I. N. Odeh, Y. Wu and P. M. Ajayan, Cryo-mediated exfoliation and fracturing of layered materials into 2D quantum dots, *Sci. Adv.*, 2017, **3**, e1701500.

14 R. Liu, D. Wu, X. Feng and K. Muellen, Bottom-up fabrication of photoluminescent graphene quantum dots with uniform morphology, *J. Am. Chem. Soc.*, 2011, **133**, 15221.

15 D. Pan, J. Zhang, Z. Li and M. Wu, Hydrothermal route for cutting graphene sheets into blue-luminescent graphene quantum dots, *Adv. Mater.*, 2010, **22**, 734.

16 L. Lin, Y. Xu, S. Zhang, I. M. Ross, A. C. M. Ong and D. A. Allwood, Fabrication and luminescence of monolayered boron nitride quantum dots, *Small*, 2014, **10**, 60.

17 V. Nicolosi, M. Chhowalla, M. G. Kanatzidis, M. S. Strano and J. N. Coleman, Liquid exfoliation of layered materials, *Science*, 2013, **340**, 1226419.
18 S. Bertolazzi, J. Brivio and A. Kis, Stretching and breaking of ultrathin MoS_2, *ACS Nano*, 2011, **5**, 9703.
19 C. Lee, X. Wei, J. W. Kysar and J. Hone, Measurement of the elastic properties and intrinsic strength of monolayer graphene, *Science*, 2008, **321**, 385.
20 A. Falin, Q. Cai, E. J. G. Santos, D. Scullion, D. Qian, R. Zhang, Z. Yang, S. Huang, K. Watanabe, T. Taniguchi, M. R. Barnett, Y. Chen, R. S. Ruoff and L. H. Li, Mechanical properties of atomically thin boron nitride and the role of interlayer interactions, *Nat. Commun.*, 2017, **8**, 15815.
21 Y. Hernandez, V. Nicolosi, M. Lotya, F. M. Blighe, Z. Sun, S. De, I. T. McGovern, B. Holland, M. Byrne, Y. K. Gun'Ko, J. J. Boland, P. Niraj, G. Duesberg, S. Krishnamurthy, R. Goodhue, J. Hutchison, V. Scardaci, A. C. Ferrari and J. N. Coleman, High-yield production of graphene by liquid-phase exfoliation of graphite, *Nat. Nanotechnol.*, 2008, **3**, 563.
22 X. Zhang, H. Xie, Z. Liu, C. Tan, Z. Luo, H. Li, J. Lin, L. Sun, W. Chen, Z. Xu, L. Xie, W. Huang and H. Zhang, Black phosphorus quantum dots, *Angew. Chem., Int. Ed.*, 2015, **54**, 3653.
23 H. Jin, B. Baek, D. Kim, F. Wu, J. D. Batteas, J. Cheon and D. H. Son, Effects of direct solvent-quantum dot interaction on the optical properties of colloidal monolayer WS_2 quantum dots, *Nano Lett.*, 2017, **17**, 7471.
24 Y. Hong, J. W. Y. Lam and B. Z. Tang, Aggregation-induced emission: phenomenon, mechanism and applications, *Chem. Commun.*, 2009, 4332.
25 L. Cao, M. J. Meziani, S. Sahu and Y. P. Sun, Photoluminescence properties of graphene versus other carbon nanomaterials, *Acc. Chem. Res.*, 2013, **46**, 171.
26 A. Splendiani, L. Sun, Y. Zhang, T. Li, J. Kim, C. Y. Chim, G. Galli and F. Wang, Emerging photoluminescence in monolayer MoS_2, *Nano Lett.*, 2010, **10**, 1271.
27 M. E. Mackay, A. Tuteja, P. M. Duxbury, C. J. Hawker, B. Van Horn, Z. Guan, G. Chen and R. S. Krishnan, General strategies for nanoparticle dispersion, *Science*, 2006, **311**, 1740.
28 M. Palummo, M. Bernardi and J. C. Grossman, Exciton radiative lifetimes in two-dimensional transition metal dichalcogenides, *Nano Lett.*, 2015, **15**, 2794.
29 Q. Bao, H. Zhang, Y. Wang, Z. Ni, Y. Yan, Z. X. Shen, K. P. Loh and D. Y. Tang, Atomic-layer graphene as a saturable absorber for ultrafast pulsed lasers, *Adv. Funct. Mater.*, 2009, **19**, 3077.
30 Q. Bao, H. Zhang, Z. Ni, Y. Wang, L. Polavarapu, Z. Shen, Q. H. Xu, D. Tang and K. P. Loh, Monolayer graphene as a saturable absorber in a mode-locked laser, *Nano Res.*, 2011, **4**, 297.
31 F. Wang, A. G. Rozhin, V. Scardaci, Z. Sun, F. Hennrich, I. H. White, W. I. Milne and A. C. Ferrari, Wideband-tuneable, nanotube mode-locked, fibre laser, *Nat. Nanotechnol.*, 2008, **3**, 738.
32 S. Wang, H. Yu, H. Zhang, A. Wang, M. Zhao, Y. Chen, L. Mei and J. Wang, Broadband few-layer MoS_2 saturable absorbers, *Adv. Mater.*, 2014, **26**, 3538.
33 K. Wu, X. Zhang, J. Wang, X. Li and J. Chen, WS_2 as a saturable absorber for ultrafast photonic applications of mode-locked and q-switched lasers, *Opt. Express*, 2015, **23**, 11453.
34 Y. Zhang, J. J. Wang, K. E. Ballantine, P. R. Eastham and W. J. Blau, Hybrid plasmonic nanostructures with unconventional nonlinear optical properties, *Adv. Opt. Mater.*, 2014, **2**, 331.
35 W. Stöber, A. Fink and E. Bohn, Controlled growth of monodisperse silica spheres in the micron size range, *J. Colloid Interface Sci.*, 1968, **26**, 62.